7-25-2016

Controls on Turbulent Mixing in a Strongly Stratified and Sheared Tidal River Plume

Joseph T. Jurisa
Portland State University

Jonathan Nash
Oregon State University

James N. Moum
Oregon State University

Levi F. Kilcher
National Renewable Energy Laboratory

Citation Details

Jurisa, J. T., Nash, J. D., Moum, J. N., Kilcher, L. F., Jurisa, J. T., Nash, J. D., … Kilcher, L. F. (2016). Controls on Turbulent Mixing in a Strongly Stratified and Sheared Tidal River Plume. Journal of Physical Oceanography, 46(8), 2373–2388.

Controls on Turbulent Mixing in a Strongly Stratified and Sheared Tidal River Plume

JOSEPH T. JURISA,[a] JONATHAN D. NASH, AND JAMES N. MOUM

Oregon State University, Corvallis, Oregon

LEVI F. KILCHER

National Renewable Energy Laboratory, Golden, Colorado

(Manuscript received 17 August 2015, in final form 4 May 2016)

ABSTRACT

Considerable effort has been made to parameterize turbulent kinetic energy (TKE) dissipation rate ε and mixing in buoyant plumes and stratified shear flows. Here, a parameterization based on Kunze et al. is examined, which estimates ε as the amount of energy contained in an unstable shear layer ($\mathrm{Ri} < \mathrm{Ri}_c$) that must be dissipated to increase the Richardson number $\mathrm{Ri} = N^2/S^2$ to a critical value Ri_c within a turbulent decay time scale. Observations from the tidal Columbia River plume are used to quantitatively assess the relevant parameters controlling ε over a range of tidal and river discharge forcings. Observed ε is found to be characterized by Kunze et al.'s form within a factor of 2, while exhibiting slightly decreased skill near $\mathrm{Ri} = \mathrm{Ri}_c$. Observed dissipation rates are compared to estimates from a constant interfacial drag formulation that neglects the direct effects of stratification. This is found to be appropriate in energetic regimes when the bulk-averaged Richardson number Ri_b is less than $\mathrm{Ri}_c/4$. However, when $\mathrm{Ri}_b > \mathrm{Ri}_c/4$, the effects of stratification must be included. Similarly, ε scaled by the bulk velocity and density differences over the plume displays a clear dependence on Ri_b, decreasing as Ri_b approaches Ri_c. The Kunze et al. ε parameterization is modified to form an expression for the nondimensional dissipation rate that is solely a function of Ri_b, displaying good agreement with the observations. It is suggested that this formulation is broadly applicable for unstable to marginally unstable stratified shear flows.

1. Introduction

Many rivers produce strongly stratified and sheared surface-trapped plumes during the release of buoyant fluid from the estuary into the coastal ocean. In tidally forced systems, the strongest turbulence occurs during each ebb pulse, with the associated mixing and horizontal advection acting to set the character of the system, referred to here as a tidal river plume (Fig. 1). These flows are observed to be highly turbulent, with the turbulent kinetic energy (TKE) dissipation rate ε exceeding $10^{-3}\,\mathrm{W\,kg^{-1}}$ in the region near the mouth of the river (e.g., MacDonald et al. 2007, hereinafter MGH07; Nash et al. 2009; Kilcher et al. 2012). The turbulence appears to be generated by Kelvin–Helmholtz (KH)-type instabilities (i.e., Geyer and Farmer 1989; Geyer et al. 2010; MacDonald and Geyer 2004, hereinafter MG04), which are initiated when the Richardson number $\mathrm{Ri} = N^2/S^2$ drops below a critical value Ri_c, often found to be 0.25 (e.g., Miles 1961). Here, $N^2 = -(g/\rho_o)(\partial\rho/\partial z)$ is the squared buoyancy frequency, and $S^2 = (\partial u/\partial z)^2$ is the squared velocity shear. The KH instabilities extract energy from the mean flow to turbulence, resulting in the mixing and vertical redistribution of density and momentum. This reduces both S^2 and N^2, but S^2 more rapidly (assuming a turbulent Prandtl number equal to 1), thereby increasing the stability of the system by increasing Ri. Above $\mathrm{Ri} = \mathrm{Ri}_c$, the stabilizing effects of the stratification act to suppress the destabilizing effects of the velocity shear, so there is no direct mechanism for turbulence generation. The amount of energy released during any particular turbulent event is set by the reduced shear ($S^2 - N^2/\mathrm{Ri}_c$), defined as the

[a] Current affiliation: Portland State University, Portland, Oregon.

Corresponding author address: Joseph T. Jurisa, Maseeh College of Engineering and Computer Science, Portland State University, 1930 SW 4th Ave., Suite 200, Portland, OR 97201.
E-mail: jurisa@pdx.edu

DOI: 10.1175/JPO-D-15-0156.1

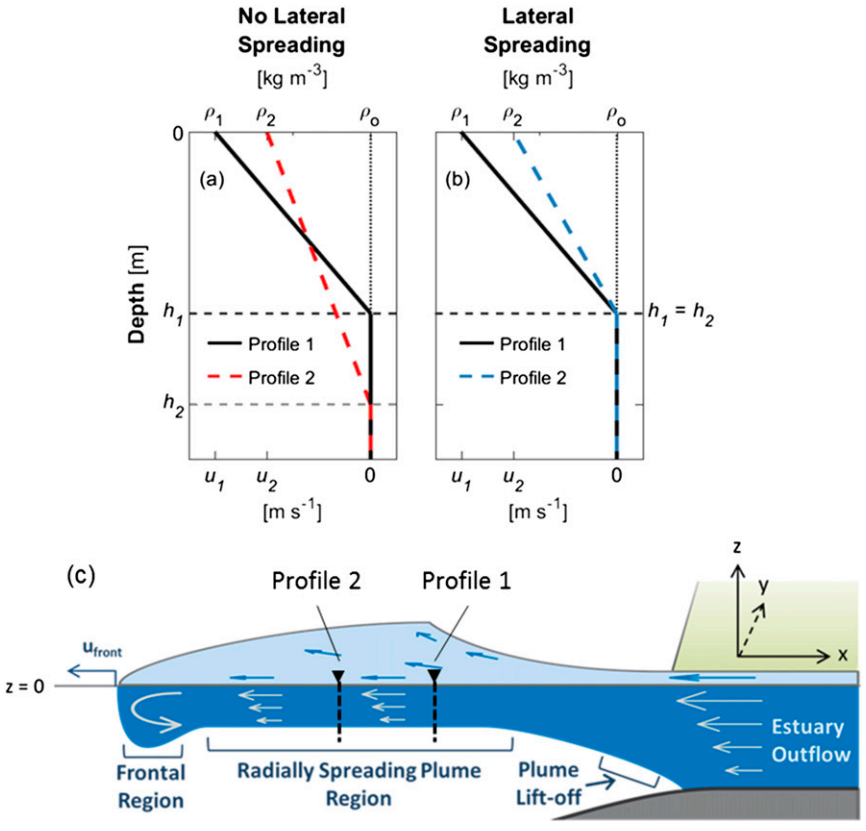

FIG. 1. Idealized vertical structure of u (lower x axes) and ρ (upper x axes): (a) in the absence of lateral spreading and (b) with lateral plume spreading. (c) Slice through a schematic of a buoyant tidal river plume. Plume spreads offshore from right to left. Offshore directed velocities are negative. The subscripts 1 and 2 in (a) and (b) mark the profile location in (c). Profile 1 is an initial profile, and profile 2 is located further offshore and is the result of mixing profile 1. In (a) and (b), h_1 and h_2 mark the plume depth before and after a mixing event.

difference in available shear versus the shear associated with that of the stabilized mixed flow. Turbulence existing in flows where $\mathrm{Ri} > \mathrm{Ri}_c$ is likely the result of decaying turbulence, the advection of turbulence, and/or the generation of turbulence by unstable shear layers at scales smaller than the sampling resolution (e.g., Rohr et al. 1988; Itsweire et al. 1993; Polzin 1996; Smyth et al. 2001).

The purpose of this study is to examine the relationship between ε, S^2, and N^2 to quantify the effectiveness of various parameterized forms for the dissipation rate and to assess how these act to set the structure and composition of an energetic tidal river plume. Previous attempts to parameterize ε in tidal river plumes have led to a formulation based on the plume's bulk velocity difference, thickness, and an interfacial drag coefficient C_{di} (MG04; MGH07). For the simplest case of constant C_{di}, the effect of stratification on altering the turbulence is ignored. We show here that an interfacial drag parameterization using $C_{\mathrm{di}} \approx 5 \times 10^{-4}$ from MG04 can be appropriate for the highly energetic regions of a tidal river plume, similar to the lift-off regions of the Fraser and Merrimack River plumes (MG04; MGH07). This value of C_{di} tends to overestimate ε in the less energetic regions of parameter space where stratification plays a first-order role in controlling the amount of energy released in returning the system to a stable state ($\mathrm{Ri} \geq \mathrm{Ri}_c$). It was noted by MG04 and MGH07 that C_{di} likely varies according to Ri, but the Ri parameter space captured by those studies was insufficient to ascertain any Ri dependence. Alternatively, MacDonald and Chen (2012) posited that an additional vortex stretching mechanism driven by lateral spreading contributed to the elevated C_{di} values in addition to the role of the bulk stratification and shear. Thus, it was argued that $C_{\mathrm{di}} = 5 \times 10^{-4}$ observed in the lift-off regions of the Fraser and Merrimack tidal plumes is a spreading-influenced value, and C_{di} decreases as the influence of the lateral spreading-induced vortex stretching mechanism is reduced (MacDonald and Chen 2012).

In the following, we investigate the dependencies of ε on both N^2 and S^2 in a tidal plume. Based on the

distribution of the data, we conclude that stratification can have $O(1)$ effects on the dissipation rate and thus requires alternate forms for its parameterization. Here, we consider a parameterization for ε developed by Kunze et al. (1990, hereinafter KWB) and updated in Kunze (2014). The KWB parameterization was developed to estimate ε in unstable ($\mathrm{Ri} < \mathrm{Ri}_c$) shear layers from observations of N^2 and S^2 with 1–10-m sampling resolutions and has compared favorably to turbulence estimates from microstructure observations of unstable shear layers in the open ocean (KWB; Polzin 1996; Peters et al. 1995) and in some continental shelf regimes (MacKinnon and Gregg 2005) where the shear and stratification associated with the instability were sufficiently resolved. In the case of MacKinnon and Gregg (2005), the unstable shear was associated with the passage of large-amplitude internal waves. Here, we find it is also aptly suited for strongly forced tidal plume systems, which are often marginally unstable ($\mathrm{Ri} < \mathrm{Ri}_c$) over a significant fraction of the plume thickness (Nash et al. 2009). The KWB parameterization is based on a local competition between the stabilizing influence of stratification and the destabilizing influence of velocity shear and only requires knowledge of the local velocity and density gradients, along with the thickness of the unstable shear layer. There are numerous alternate ways to parameterize ε; the KWB parameterization is utilized here since the Columbia River tidal plume observations resolve the unstable shear layer in the plume.

The conceptual tidal plume system considered here is described in section 2 along with the derivations of the KWB ε parameterization and the interfacial drag parameterization utilized by MG04. The observational data from the tidal Columbia River plume are described in section 3 and will be compared to the two ε parameterizations in sections 4 and 5. The validity of a constant interfacial drag coefficient and scaled dissipation rate is discussed in section 6, and the results are summarized in section 7.

2. Parameterizing ε in a marginally unstable ($\mathrm{Ri} < \mathrm{Ri}_c$) tidal plume

a. Conceptual buoyant tidal plume structure

The structure of an idealized tidal plume is depicted in Fig. 1. During ebb tide, relatively fresh, buoyant fluid is discharged from the estuary into a coastal ocean assumed to be quiescent and with uniform density ρ_o. Offshore from the estuary, a stratified and sheared buoyant plume forms that spreads laterally because of the cross-axis pressure gradients and the absence of the lateral boundaries of the estuary. Conservation of mass and momentum leads the plume to detach or lift-off from the bottom; past the lift-off region, the plume is considered to be a freely propagating, radially spreading gravity current (Fig. 1c; Kilcher and Nash 2010). It is the core of this stratified and sheared radially spreading plume region that is the focus of this study.

Vertical profiles of density and velocity within the tidal plume are often observed to be nearly linear (Kilcher et al. 2012), producing approximately constant shear, stratification, and Richardson number over the plume thickness h_p, represented as h_1 and h_2 in Figs. 1a and 1b. A bulk Richardson number can then be defined as $\mathrm{Ri}_b = g'h_p/\Delta u^2$, which describes the overall stability within the plume. Here, the reduced gravity $g' = (g/\rho_o)/(\rho_o - \rho)$ and Δu represent the total density and velocity difference over h_p, respectively. While the discrete nature of this form draws from a two-layer conceptual model, here we explicitly use this to describe a continuously stratified/sheared system. Previous work on laboratory-scale spreading plumes (Yuan and Horner-Devine 2013) and the tidal plumes of the Merrimack (MGH07) and Columbia Rivers (Kilcher and Nash 2010) reveal that this general assumption of nearly linear velocity and density profiles and correspondingly nearly constant shear and stratification is reasonable.

For a plume with initially unstable Ri_b ($\mathrm{Ri}_b < \mathrm{Ri}_c$), turbulent mixing entrains low-momentum/high-density ambient fluid into the plume. In the absence of lateral spreading, the entrainment of ambient fluid increases the bulk stability of the plume Ri_b by increasing the plume thickness and decreasing S^2 disproportionately more than N^2 (Fig. 1a). The stabilizing effect of mixing is counteracted by lateral spreading, which thins the plume, intensifying S^2 more rapidly than N^2, thereby reducing Ri and increasing the potential for turbulence (Fig. 1b). The plume thus develops through the competition between turbulent mixing and lateral spreading, the details of which set the plume's character. Note that the lateral spreading of the plume drives a lateral divergence of the buoyant plume fluid so the buoyancy is reduced along a 2D plume streamline (Fig. 1b); buoyancy is conserved by accounting for the lateral expansion of the volume.

This conceptual system is in accordance with idealized numerical plume studies (Hetland 2010) that reported that the turbulent entrainment in a plume is a function of the plume's aspect ratio $\alpha = h_p/W$ and nondimensional lateral spreading rate dW/dz that is related to Ri_b by $dW/dx = 2\mathrm{Ri}_b^{1/2}$. As the plume simultaneously spreads in the offshore and lateral

directions, the change of Ri_b, and consequently the plume stability, varies in the offshore direction as $\partial \mathrm{Ri}_b/\partial x = f(\mathrm{Ri}_b, \alpha)$. The term α can be an important factor when comparing different tidal plume systems, as the decrease in Ri_b is larger for narrow plumes (large α) than for wide plumes (small α; Hetland 2010).

In the Merrimack River plume, MacDonald and Chen (2012) argued that a vortex stretching mechanism is an additional process that is distinctly separate from, but still complementary to, the reduction of Ri_b by the spreading-induced enhancement of S^2. It was posited that the enhancement of turbulence by vortex stretching in a laterally spreading tidal plume acts at scales smaller than those captured by Ri_b and needs to be included in the parameterization of dissipation. Consequently, for a given Ri_b, variability in turbulence can be attributed to differences in the lateral spreading and α (MacDonald and Chen 2012).

For the purpose of this study, we do not explicitly consider an additional term to account for vortex stretching. Instead we assume that the lateral spreading of the plume alters Ri_b through the preferential enhancement of S^2 relative to N^2, and thus the details of the turbulence in the Columbia River tidal plume can be described to the leading order through some local value of Ri_b. This differs from the findings of MacDonald and Chen (2012) in the Merrimack River tidal plume, as we show in the following sections turbulence in the Columbia River tidal plume can be described without the inclusion of a separate spreading parameter. The disparity in the lateral spreading influence in the Columbia and Merrimack tidal plumes is potentially brought about by the vast difference in the spatial scales of the two systems. The aspect ratio of the Columbia tidal plume is an order of magnitude smaller than that of the Merrimack, which suggests that, relative to the Merrimack, the influence of lateral spreading is small in the Columbia (MacDonald and Chen 2012). More thorough analyses on the validity of this assumption and the applicability of the KWB parameterization for tidal plumes covering a wide range of aspect ratios are needed but beyond the scope of this study.

With this conceptual framework, we now introduce and discuss parameterizations for ε using the bulk-averaged plume properties.

b. Interfacial drag coefficient parameterization

We begin by describing the ε parameterization used by MG04 and MGH07 in the tidal Fraser and Merrimack River plumes. A control volume method was initially used to estimate ε, and, motivated by Ivey and Imberger (1991) and Imberger and Ivey (1991), ε was scaled by $\Delta u g'$. MG04 subsequently developed a formulation for the normalized dissipation $\varepsilon_c/(\Delta u g')$:

$$\frac{\varepsilon_c}{\Delta u g'} = \frac{(1 - \mathrm{Ri}_f)}{\mathrm{Ri}_b} C_{\mathrm{di}}, \tag{1}$$

where C_{di} is an interfacial drag coefficient, Ri_f is the flux Richardson number (assumed to be constant), and $\mathrm{Ri}_b = g' h_p/\Delta u^2$ is the bulk Richardson number. Substituting $\mathrm{Ri}_b = g' h_p/\Delta u^2$ into (1) and rearranging terms yields an expression for the average ε_c over the plume thickness h_p:

$$\varepsilon_c = (1 - \mathrm{Ri}_f) \frac{\Delta u^3}{h_p} C_{\mathrm{di}}. \tag{2}$$

This is the rate at which energy is extracted from the mean flow or the rate of work done by the internal stresses. The expressions in (1) and (2) are denoted by the subscript "c" and will be referred to as the interfacial drag parameterization.

In the tidal Fraser River plume, $\mathrm{Ri}_b \approx 0.2$, and scaling the observed values of ε by Δu and g', it was determined $\varepsilon/(\Delta u g') \approx 2 \times 10^{-3}$, which, from (1), yielded $C_{\mathrm{di}} = 5 \times 10^{-4}$ (MG04). Ultimately, $\varepsilon_c/(\Delta u g')$ decreased with increasing distance from the river mouth, suggesting that $\varepsilon/(\Delta u g')$ and C_{di} cannot be assumed constant in (1) and (2) for the purpose of predicting ε (MGH07). MacDonald and Chen (2012) reported that $\varepsilon_c/(\Delta u g')$ was not correlated with Ri_b for the Merrimack River tidal plume and that $\varepsilon_c/(\Delta u g')$ and C_{di} additionally varied according to a lateral spreading parameter, as noted in the previous section.

The variability in $\varepsilon/(\Delta u g')$ and C_{di} and the respective dependencies on Ri_b are described and put into context in the following sections.

c. N^2 and S^2 parameterization

The ε parameterization in (2) does not directly include the effects of stratification suppressing turbulence production, as N^2 does not appear in the formulation. Instead, the effects of stratification are incorporated into the variability of C_{di}, which either must be known or determined empirically based on assumptions for the value of $\varepsilon/(\Delta u g')$ and knowledge of the lateral plume spreading (MG04; MGH07; MacDonald and Chen 2012), which itself depends on the nature of the turbulence.

To more directly include the effects of stratification and how it may limit the energy available for turbulence, we employ the scaling for ε proposed by KWB. The KWB dissipation parameterization is formulated as a function of

TABLE 1. Length-scale definitions.

h_p	Plume thickness (m)
$L_o = (\varepsilon N^{-3})^{1/2}$	Ozmidov length scale (m)
L_T	Rms Thorpe displacement length scale (m)
$L_\delta = h_p/\delta_h$	Unstable shear layer thickness (m)
$\delta_h = 5$	Nondimensional unstable shear layer thickness scaling factor

the mean shear S, stratification N, and thickness of the unstable shear layer L_δ (Table 1):

$$\varepsilon_{\mathrm{KWB}} = (1 - \mathrm{Ri}_f) L_\delta^2 \frac{(S^2 - N^2 \mathrm{Ri}_c^{-1})(S - N\mathrm{Ri}_c^{-1/2})}{96}. \quad (3)$$

The KWB parameterization [(3)] is the product of the kinetic energy available to create a turbulent overturn $L_\delta^2(S^2 - N^2\mathrm{Ri}_c^{-1})/24$ (Thompson 1980) and an inverse time scale set by the growth rate of a Kelvin–Helmholtz instability and assumed to be $(S - N\mathrm{Ri}_c^{-1/2})/4$ (Hazel 1972). The term Ri_c is a critical Richardson number at which turbulence ceases to be sustained, which KWB set to 0.25; Polzin (1996) noted a better correlation between the KWB parameterization and observations when a larger value $\mathrm{Ri}_c \approx 0.4$ was utilized. Thereby, the KWB parameterization in (3) is the amount of energy that must be dissipated over a time scale of a KH instability to return the initially unstable shear layer to the marginally stable state: $\mathrm{Ri} = \mathrm{Ri}_c$. The KWB parameterization in (3) is further rearranged to form an expression for ε based on the bulk-averaged Richardson number of the layer (Polzin 1996; Kunze 2014)

$$\varepsilon_{\mathrm{KWB}} = (1 - \mathrm{Ri}_f) N^3 L_\delta^2 \frac{(\mathrm{Ri}_b^{-1} - \mathrm{Ri}_c^{-1})(\mathrm{Ri}_b^{-1/2} - \mathrm{Ri}_c^{-1/2})}{96}. \quad (4)$$

Here, the shear and stratification are used to formulate the bulk-averaged Richardson number $\mathrm{Ri}_b = \langle N^2 \rangle / \langle S^2 \rangle$, with angle brackets $\langle \cdot \rangle$ denoting averages taken over the thickness of the shear layer; Ri_b is related to the Froude number in Kunze (2014) and Polzin (1996) as $\mathrm{Ri}_b = \mathrm{Fr}^{-1/2}$.

We should point out here that there is some ambiguity in defining the length scale L_δ in (4), which might be assumed to scale with the plume thickness h_p, since this sets the vertical scale of unstable shear (Kunze 2014). We investigate the relationship between L_δ and h_p in more detail in the following section. For now we assume that $L_\delta = h_p/\delta_h$, with δ_h as a constant scaling factor (Table 1). While in general Δu and g' are computed as differences over h_p, in the following sections L_δ is also used as a length scale over which to compute Δu and g', which we differentiate by denoting with $(\cdot)_\delta$.

In the following, we show that (2) and (4) are equivalent if C_{di} is allowed to be variable, which from (2) is $C_{\mathrm{di}} = \varepsilon(\Delta u^3/h)^{-1}(1 - \mathrm{Ri}_f)^{-1}$. Since $(\Delta u^3/h)_\delta = N^3 L_\delta^2 \mathrm{Ri}_b^{-3/2}$, (4) can be divided by $(\Delta u^3/h)_\delta$ to yield an expression for the interfacial drag coefficient from the KWB parameterization:

$$C_{\mathrm{KWB}} = \mathrm{Ri}_b^{3/2} \frac{(\mathrm{Ri}_b^{-1} - \mathrm{Ri}_c^{-1})(\mathrm{Ri}_b^{-1/2} - \mathrm{Ri}_c^{-1/2})}{96}. \quad (5)$$

In (5) we now have an expression for the interfacial drag coefficient that is dependent solely on the bulk-averaged Ri of the layer. We note that since C_{KWB} in (5) utilizes L_δ and not h_p, it must be scaled by δ_h^2 to be comparable to C_{di} in (2).

The nondimensional scaling for ε utilized by MG04 and MGH07 in (1) is then recovered by dividing (4) by $(\Delta u g')_\delta = N^3 L_\delta^2 \mathrm{Ri}_b^{-1/2}$:

$$\frac{\varepsilon_{\mathrm{KWB}}}{(\Delta u g')_\delta} = \mathrm{Ri}_b^{1/2}(1 - \mathrm{Ri}_f) \frac{(\mathrm{Ri}_b^{-1} - \mathrm{Ri}_c^{-1})(\mathrm{Ri}_b^{-1/2} - \mathrm{Ri}_c^{-1/2})}{96}. \quad (6)$$

As (6) utilizes the length scale L_δ, it must be scaled by δ_h^2 when comparing to the values from MG04 and MGH07 that calculated the bulk velocity and density differences over h_p (e.g., $\delta_h^2(\Delta u g')_\delta = \Delta u g'$).

The KWB parameterizations in (5) and (6) indicate that C_{KWB} and $\varepsilon_{\mathrm{KWB}}/(\Delta u g')_\delta$ should vary with Ri_b, as suggested by MG04 and MGH07, and in part motivates our desire to elucidate the roles of N^2, S^2, and L_δ in controlling the turbulence and structure of the tidal river plume.

THE UNSTABLE SHEAR LAYER LENGTH SCALE L_δ

Kunze (2014) defined L_δ as the thickness of the unstable shear ($\mathrm{Ri}_b < \mathrm{Ri}_c$) layer and related it to the Ozmidov length scale $L_o = (\varepsilon N^{-3})^{1/2}$, which represents the outer limits of turbulence scales by dividing (4) by $N^3 L_\delta^2$:

$$\frac{\varepsilon}{N^3 L_\delta^2} = \left(\frac{L_o}{L_\delta}\right)^2 = (1 - \mathrm{Ri}_f) \frac{(\mathrm{Ri}_b^{-1} - \mathrm{Ri}_c^{-1})(\mathrm{Ri}_b^{-1/2} - \mathrm{Ri}_c^{-1/2})}{96}. \quad (7)$$

Thus, the separation between the unstable shear layer thickness L_δ and the largest turbulence scale L_o depends on how unstable the shear layer is (Kunze 2014). Assuming $\mathrm{Ri}_c = 0.5$ and $\mathrm{Ri}_f = 0.17$, L_o is less than L_δ over the range $0.033 < \mathrm{Ri}_b < \mathrm{Ri}_c$.

If we consider a theoretical overturn spanning a thickness h_T, the resulting rms Thorpe displacements are $L_T = h_T/6$ (Thorpe 2010). By assuming $L_o \approx L_T$ and $\varepsilon = N^3 L_T^2$, it is seen in (7) that for $(L_o/L_\delta)^2 \approx 1$, $L_\delta \approx L_o \approx h_T/6$. In the context of the tidal plume system considered here, $h_T \approx h_p$, meaning the maximum overturning length scale is set by the plume thickness. This results in the definition for shear layer thickness for the KWB parameterization $L_\delta = h_p/\delta_h$, with δ_h as a scaling factor (Table 1).

It is likely that the actual value of δ_h is dependent on other factors, such as the choice of Ri_c, the definition of h_p, and the vertical structure of velocity and density that is assumed (e.g., Hazel 1972). A more thorough examination of the relevant length scales is needed but is beyond the scope of this study. For now, δ_h is treated as a constant scaling factor, and it is shown in the following sections that a value of $\delta_h = 5$ yields good agreement with the observations.

3. Data and methods

To better understand the dynamics controlling the variability in ε, the parameterizations described above are compared to observations of ε in the tidal Columbia River plume collected as part of the larger River Influences on Shelf Ecosystems (RISE) project (Hickey et al. 2010). The dataset has been previously used to describe the tidal plume's frontal structure and propagation (Kilcher and Nash 2010), momentum balance (Kilcher et al. 2012), and the dependencies of the near-field structure on tidal and river forcings (Nash et al. 2009). We refer the reader to these studies for a more thorough description of the measurements than is warranted here.

a. Setting

Sampling spanned 8–14 and 18–26 August 2005 and 22 and 26–31 May 2006, which covered a range of tidal forcing and river discharge Q_R (Fig. 2). The sampling period captured the spring tide and spring–neap tide transition, with the amplitude of the depth-averaged ebb tidal velocities u_{tide} ranging from 1 to 2.5 m s^{-1}. The August 2005 period occurred during low discharge conditions with Q_R varying between 3000 and 4500 m^3 s^{-1}, and the May 2006 period occurred during the spring freshet with Q_R varying between 13 000 and 14 000 m^3 s^{-1}.

b. Sampling strategy and methods

Repeated shipboard transects through the tidal plume were conducted aboard the R/V *Point Sur* along three transect lines: line 4 running east–west between −2 and −20 km offshore of the mouth of the Columbia River (MCR) and lines 0 and 1 running generally north–south and intersecting line 4 around −2 and −5.25 km offshore of the MCR, respectively (Fig. 2a). Lines 1 and 4 were sampled in both years, while line 0 was only sampled over a 2-day period in 2005.

Two sampling strategies were employed along the transect lines: a front-tracking mode and repeat-transect time series, in which a short line segment was repeated every hour or two over a period consisting of at least one tidal cycle, with vertical profiles of turbulence obtained every 1–2 min. Time series transects conducted along line 4 spanned −4 to −10 km offshore (Fig. 2a, solid blue line). Front-tracking surveys were carried out during the August 2005 field effort and involved following and conducting transects through the frontal region of 7 tidal plumes as they propagated offshore. The fronts were generally tracked between −4 and −25 km offshore of the MCR along line 4 (Fig. 2a).

For all the surveys analyzed, vertical profiles of temperature, salinity, and velocity shear microstructure were continually collected while underway using the Chameleon microstructure profiler (Moum et al. 1995). Chameleon was deployed on a loose tether approximately 5 m off the starboard side using the ship's crane in an effort to avoid contamination from the ship's wake. Still, we omit the upper 3 m of data from this analysis due to potential ship-wake contamination and the changing orientation and acceleration of the profiler. The TKE dissipation rate ε is calculated by matching the variance of the observed shear spectra measured by Chameleon's shear probes to the theoretical spectra over 1-m bins (Moum et al. 1995). Salinity and temperature are averaged over 1-m bins to match the resolution of the ε data.

Velocity measurements used for this analysis were collected using a 1200-kHz RDI acoustic Doppler current profiler (ADCP) mounted over the side of the ship. The ADCP sampled with a 0.5-m vertical bin size with the first good bin located at 2.2 m.

Profiles of N^2 are calculated using the resorted 1-m binned density profiles from Chameleon. The 1-m velocity shear squared $S^2 = (\partial u/\partial z)^2 + (\partial v/\partial z)^2$ is calculated at the Chameleon profile location from the 1200-kHz ADCP velocity data, which is first converted to 1-m vertical bins to match the vertical resolution of the ε data.

The subsequent analysis is carried out using data collected along lines 0 and 1, spanning the range $-0.5 < y < 0.5$ km and line 4. Data collected along line 4 are separated into three regions. For the time series surveys, line 4 is divided into two subsections, lines 4.1 and 4.2, covering the cross-shore distances $-7 < x < -4$ km and $-10 < x < -7$ km,

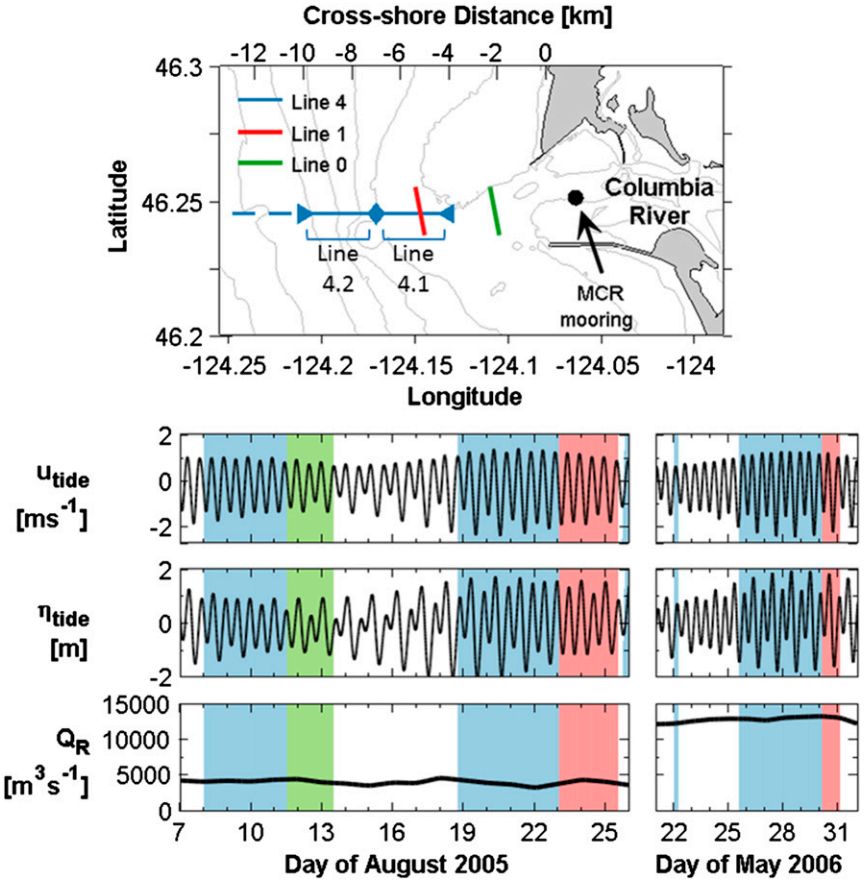

FIG. 2. (a) Map of study area. Transect lines are plotted in color. The solid blue line represents the area of line 4 where the time series transects were conducted. The two averaging regions along line 4, lines 4.1 and 4.2, are bracketed by inward-pointing triangles (> <). The dashed blue line marks the front-tracking transects along line 4, conducted out to −25 km offshore. Time series of tidal velocity u_{tide}, elevation η_{tide}, and river discharge Q_R are plotted in the lower panels for both the August 2005 and May 2006 study periods. Colored regions in time series panels correspond to the transect lines depicted in the map that are sampled during that period.

respectively (Fig. 2a). Additionally, the data utilized here from the front-tracking surveys along line 4 are restricted to the area 0.4–2.5 km inshore of the tidal plume front. Following previous Columbia River plume studies, the plume depth h_p is defined as the depth where the cross-shore (plume) velocity is 1/3 of the near-surface value (Kilcher and Nash 2010; Kilcher et al. 2012). Because of the lack of data in the upper 3 m of the water column, data averaged over the plume thickness are averaged over the depth range $-h_p \leq z \leq -3$ m. Because of this restricted range, h_p is required be larger than 6 m for an average to be included in the analysis.

Profile averages, denoted with angle brackets and the subscript "profile" (i.e., $\langle\cdot\rangle_{\text{profile}}$), are taken over three consecutive profiles. Transect averages, denoted simply by angle brackets $\langle\cdot\rangle$, are taken over one of the transect segments defined above. For instances when the front is located in the transect regions of line 4.1 and 4.2, only the stratified and sheared region behind the front are included in the transect and profile averages. An example of this can be seen in Fig. 3, which depicts a transect through the plume along line 4.1. A frontal feature is observed near $x = -5.5$ km. Averages for this transect are then taken over the distance $-5.25\text{ km} < x < -4\text{ km}$.

4. Dependence of ε on plume structure

The turbulence in the Columbia River plume's near field is controlled by the magnitude of the river freshwater discharge Q_R and tidal forcing, which ultimately influence the structure of the near-field plume (Nash et al. 2009). To highlight the dependencies of ε on the tidal plume structure, we briefly

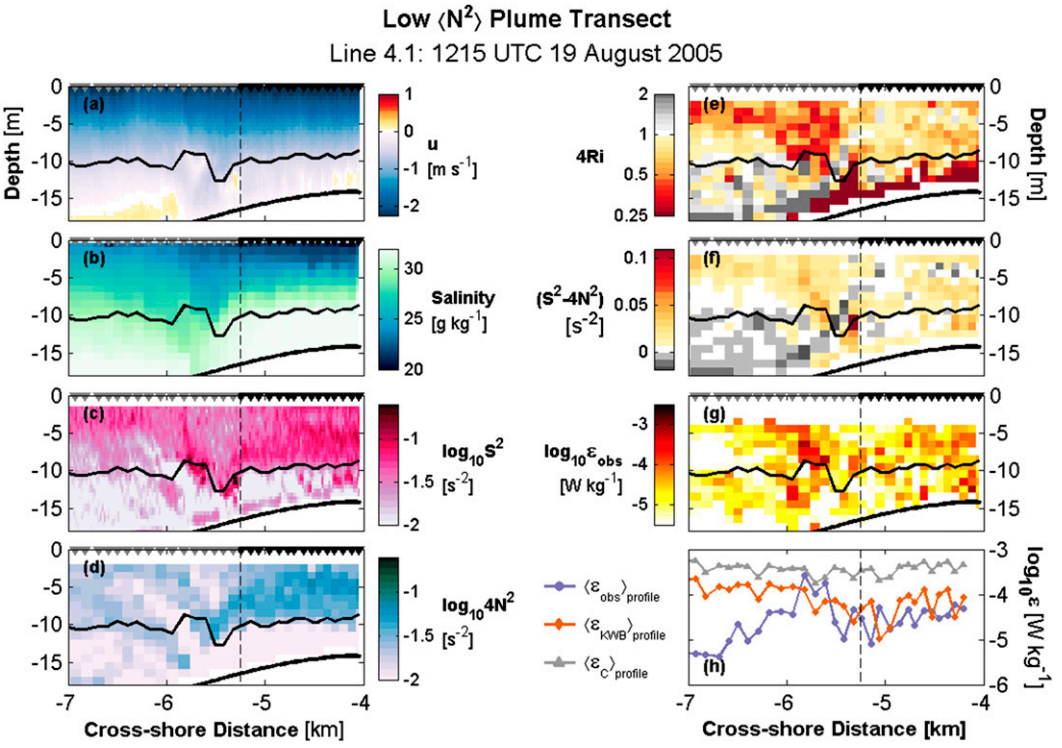

FIG. 3. Observations of a low $\langle N^2 \rangle$ plume taken along line 4.1 on 19 Aug 2005. (a) Cross-shore velocity. Profiles of (b) salinity, (c) S^2, (d) N^2, (e) 4Ri, (f) $S^2 - 4N^2$, (g) $\varepsilon_{\rm obs}$, and (h) $\langle \varepsilon_{\rm obs} \rangle_{\rm profile}$, $\langle \varepsilon_{\rm KWB} \rangle_{\rm profile}$, and $\langle \varepsilon_c \rangle_{\rm profile}$. Black line in (a)–(g) marks the plume depth. Triangles above (a)–(g) mark locations of profiles. Black triangles mark the horizontal averaging region for the transect, also marked by the vertical dashed line in all panels.

describe the contrasting structure and turbulence of two tidal plumes with similar Ri_b values.

a. Plumes with similar Ri_b and differing N^2 and h_p

Two representative transects along transect line 4 taken on 19 August 2005 and 29 May 2006 are used here to highlight dependencies of ε on the plume structure (Figs. 3–5; Table 2). The two transects capture ebb tides of similar tidal strength and duration. They were conducted during similar stages of the tidal evolution. The main difference in forcing is the nearly fourfold difference in Q_R for the two sampling periods (Table 2). The higher river discharge for May 2006 leads to a thinner tidal plume that has stronger stratification, $h_p = 7.4$ m and $\langle N^2 \rangle = 0.02\,\mathrm{s}^{-2}$ (Table 2; Figs. 4, 6), compared to the plume from August 2006, $h_p = 9.7$ m and $\langle N^2 \rangle = 0.009\,\mathrm{s}^{-2}$ (Table 2; Figs. 3, 5). The difference between $\langle N^2 \rangle$ is compensated by the factor of 2 difference between $\langle S^2 \rangle$ to yield similar values for the bulk Richardson number Ri_b ($\mathrm{Ri}_b = 0.2$ for the August 2005 transect, and $\mathrm{Ri}_b = 0.16$ for the May 2006 transect). Local values of the gradient Richardson number are similar for both transects with $\mathrm{Ri} \leq 0.25$ above the plume base (Figs. 3c, 4c). Velocity and salinity profiles vary approximately linearly with depth, so that S^2 and N^2 are nearly constant (Figs. 5, 6) and typically within a factor of 2 of their transect- and vertically averaged values, consistent with our conceptual plume model (Fig. 1).

While Ri_b is similar for the two transects, the dissipation rates differ by an order of magnitude, with $\langle \varepsilon_{\rm obs} \rangle = 3.8 \times 10^{-4}\,\mathrm{W\,kg^{-1}}$ for the high $\langle N^2 \rangle$ May 2006 transect and $\langle \varepsilon_{\rm obs} \rangle = 3.5 \times 10^{-5}\,\mathrm{W\,kg^{-1}}$ for the low $\langle N^2 \rangle$ August 2005 transect (Figs. 3e, 4e). This order-of-magnitude difference in $\varepsilon_{\rm obs}$ for two periods with equivalent Ri_b highlights the inadequacy of using Ri_b as a sole parameter to predict ε. The reduced shear ($S^2 - N^2/\mathrm{Ri}_c$) is a better metric for the turbulence intensity in this instance (Figs. 3, 4; Table 2), but since it neglects h_p, it can fail for systems that have similar reduced shear but differing h_p.

b. Dependency of ε on N^2, S^2, and h_p

In the following, we explore the variability of ε in the N^2, S^2, and h_p parameter space. For this comparison, all valid profile averages from both 2005 and 2006 located within the averaging regions on transect lines 0, 1, and 4 (Fig. 2a) are bin averaged in $\langle N^2 \rangle_{\rm profile}$,

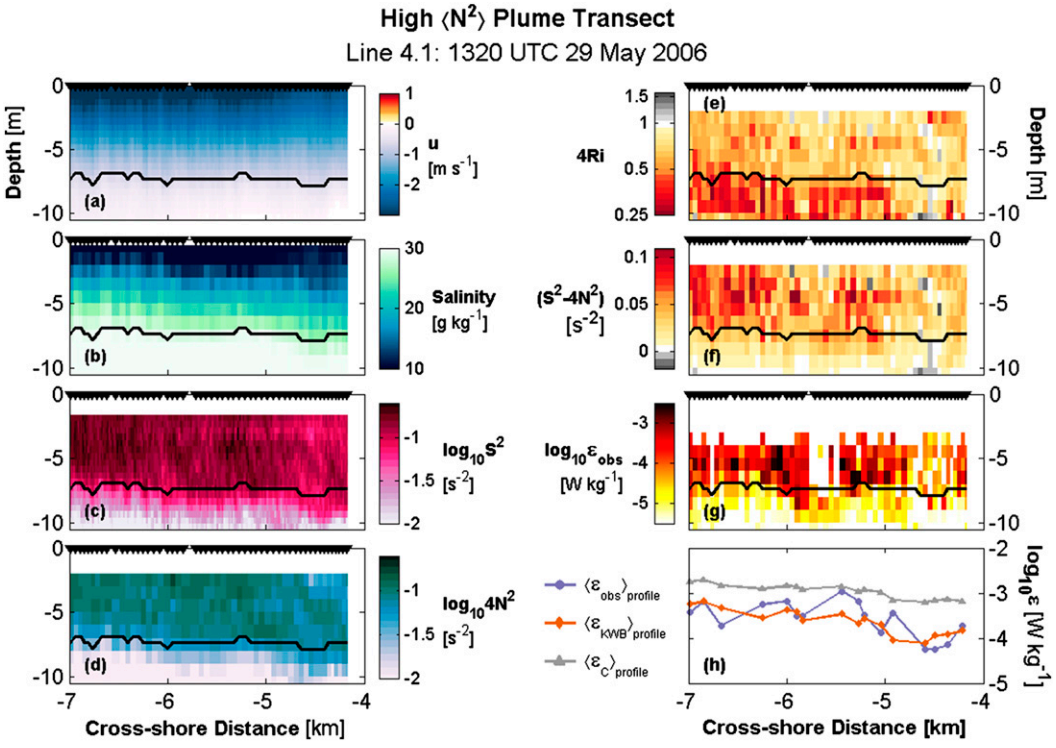

FIG. 4. As in Fig. 3, but for a transect taken through a high $\langle N^2 \rangle$ plume along line 4.1 on 29 May 2006. Note the changes in the y axis and color bar limits.

$\langle S^2 \rangle_{\text{profile}}$, and h_p space. For the S^2 and N^2 dimensions, there are eight bins per decade in $\log_{10}$ space and the h_p dimension consists of 3-m bins over the interval $6\,\text{m} \le h_p \le 15\,\text{m}$. A minimum of three independent profile averages are required for a valid bin-averaged value (e.g., at least nine profiles go into each bin average). The bin-averaged $\langle \varepsilon_{\text{KWB}} \rangle_{\text{profile}}$ is computed from (5) using the bin-averaged $\langle N^2 \rangle_{\text{profile}}$, $\langle S^2 \rangle_{\text{profile}}$, and h_p values.

From the bin averages in the N^2, S^2, and h_p parameter space, the highest values of $\langle \varepsilon_{\text{obs}} \rangle_{\text{profile}}$ tend to be located in regions with both high N^2 and S^2 and with thinner h_p (Fig. 7b). Thicker plumes generally reside in the regions of lower N^2 and S^2 (Fig. 7d). The magnitude of $\langle \varepsilon_{\text{obs}} \rangle_{\text{profile}}$ decreases as Ri_b approaches Ri_c in agreement with the KWB parameterization, though turbulence still exists for $\text{Ri}_b > \text{Ri}_c$, while the KWB parameterization is undefined.

5. Comparison with theory

Here, we compare the effectiveness of the interfacial drag and KWB parameterizations in representing the observations more quantitatively.

a. *Interfacial drag coefficient formulation*

Recall that the constant drag formulation (2) is an expression for ε as a function of $\Delta u^3/h_p$ and the interfacial drag coefficient C_{di}. Even though the tidal plume can be considered strongly stratified, the effect of stratification damping ε is not explicitly included in (2) but rather is included indirectly through the value of C_{di}, if permitted to be variable.

To examine the effectiveness of the interfacial drag formulation, we start by calculating $\langle \varepsilon_c \rangle$ from the transect-averaged data using (1). For this analysis, C_{di} was assumed constant and equal to 4.2×10^{-4}. This assumption of a constant C_{di} is an oversimplification and, as is shown in the following sections, is not expected to fully capture the variability in ε over a wide range of the N^2 and S^2 parameter space. Instead it is used to highlight the importance of the bulk properties of the plume in controlling the turbulence. It will be shown in section 6 that this value for C_{di} is arrived at by taking the limit of $C_{\text{KWB}}/\delta_h^2$ in (5) as Ri_b approaches zero. This is considered an upper estimate of C_{di}, should it be allowed to vary as a function of Ri_b, and is comparable to the value of C_{di} estimated in the highly energetic lift-off region of the Fraser River plume ($C_{\text{di}} = 5 \times 10^{-4}$; MG04), though MacDonald

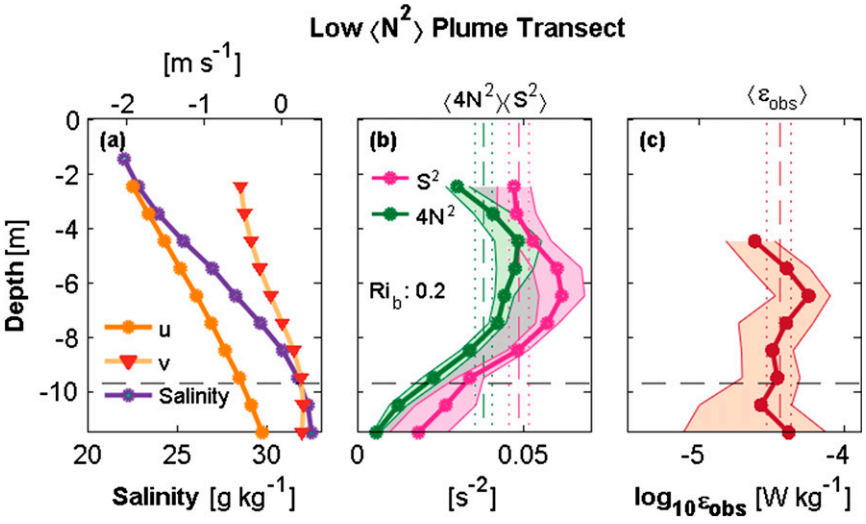

FIG. 5. Averaged profiles for the low $\langle N^2 \rangle$ plume depicted in Fig. 3; (a) u and v velocities (top x axis) along with salinity (bottom x axis), (b) $4N^2$ and S^2, and (c) ε_{obs}. Gray horizontal dashed lined indicates h_p. Light color shaded regions mark the bootstrapped 95% confidence intervals. Gray shaded region in (b) marks where $S^2 > 4N^2$ (Ri < 0.25). Vertical dashed colored lines mark the plume bootstrapped averages with the vertical dotted colored lines representing the bootstrapped 95% confidence intervals.

and Chen (2012) contend that this is a spreading impacted C_{di} value.

When compared to $\langle \varepsilon_{\text{obs}} \rangle$, the constant interfacial drag formulation does not capture the same dynamic range of variability in $\langle \varepsilon_{\text{obs}} \rangle$, as (2) has the wrong functional dependencies with a constant C_{di} and consistently overestimates $\langle \varepsilon_{\text{obs}} \rangle$ in the less turbulent regions by up to a factor of 10 (Fig. 9a). Only for the largest dissipation rates does $\langle \varepsilon_c \rangle$ agree reasonably well with $\langle \varepsilon_{\text{obs}} \rangle$ for this choice of C_{di}. Alternatively, a smaller C_{di} estimate, such as C_{di}, $= 5 \times 10^{-5}$ determined empirically by MacDonald and Chen (2012) for their nonspreading case, could have been utilized. Using C_{di}, $= 5 \times 10^{-5}$ in (2) better captures lower values of $\langle \varepsilon_{\text{obs}} \rangle$ but now underestimates $\langle \varepsilon_{\text{obs}} \rangle$ in the more energetic regimes (Fig. 9a). Changing the constant value of C_{di} only changes the magnitude of the ε_c by a constant offset and does not help to achieve the correct functional dependencies (Fig. 9a).

The Columbia River tidal plume results are consistent with the C_{di} value utilized in the Fraser River plume by MG04 for the highly energetic regions ($\text{Ri}_b \ll \text{Ri}_c$) of the tidal plume (Fig. 9a). However, for the Columbia River tidal plume dataset, Ri_b spans nearly two orders of magnitude, including less energetic periods where Ri_b approaches Ri_c. The influence of stratification on plume turbulence must be accounted for in the less energetic, marginally unstable regions through an interfacial drag coefficient that is allowed to vary as a function of Ri_b. The large range in parameter space allows for the dependencies of $\langle \varepsilon_{\text{obs}} \rangle / (\Delta u g')_\delta$, and thus C_{di}, on Ri_b to be examined in more detail, which are addressed in the following sections.

b. KWB

The observed variability in ε has different functional/power-law dependencies than what is obtained when assuming a constant value for C_{di} (Fig. 9a) and highlights the need for an ε parameterization that explicitly includes the effects of N^2, S^2, and h_p. The KWB parameterization scales with the reduced shear of the system ($S^2 - N^2 \text{Ri}_c^{-1}$) and the unstable shear layer thickness L_δ, allowing it to differentiate between thin, strongly stratified plumes and thick, weakly stratified plumes that have similar Ri_b values (i.e., Figs. 3–4; Table 2).

TABLE 2. Properties of example low and high $\langle N^2 \rangle$ plumes.

	Low $\langle N^2 \rangle$ plume, 19 Aug 2005	High $\langle N^2 \rangle$ plume, 29 May 2006
Q_R ($\text{m}^3\,\text{s}^{-1}$)	4150	13 200
$\langle N^2 \rangle$ (s^{-1})	0.0094	0.021
$\langle S^2 \rangle$ (s^{-1})	0.048	0.13
$\langle S^2 \rangle - \langle N^2 \rangle / \text{Ri}_c$ (s^{-2})	0.029	0.088
Ri_b	0.2	0.16
h_p (m)	9.7	7.3
$\langle \varepsilon_{\text{obs}} \rangle$ (W kg^{-1})	3.5×10^{-5}	3.8×10^{-4}
$\langle \varepsilon_{\text{KWB}} \rangle$ (W kg^{-1})	7.3×10^{-5}	2.4×10^{-4}
$\langle \varepsilon_c \rangle$ (W kg^{-1})	3.3×10^{-4}	8.4×10^{-4}

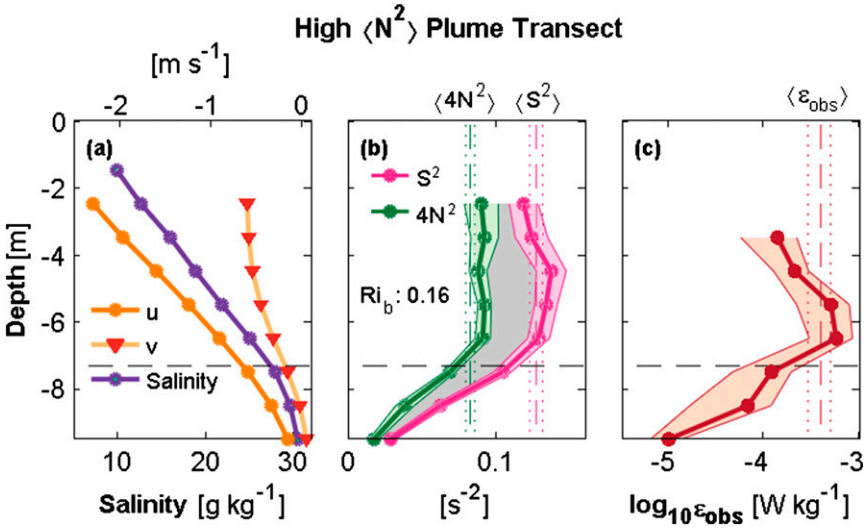

FIG. 6. As in Fig. 5, but for the high $\langle N^2 \rangle$ plume depicted in Fig. 4. Note the changes in axes limits.

Revisiting the profile averages for the representative low and high N^2 transects, $\langle \varepsilon_{\mathrm{KWB}} \rangle_{\mathrm{profile}}$ qualitatively follows $\langle \varepsilon_{\mathrm{obs}} \rangle_{\mathrm{profile}}$ for both cases (Figs. 3h, 4h). Using averages of h_p, S^2, and N^2 computed over the representative transect in (4), $\langle \varepsilon_{\mathrm{KWB}} \rangle$, is within the 95% bootstrap confidence interval of $\langle \varepsilon_{\mathrm{obs}} \rangle$, and generally no more than a factor of 2 different from the observations ($\langle \varepsilon_{\mathrm{obs}} \rangle = 3.5 \times 10^{-5}\,\mathrm{W\,kg^{-1}}$ and $\langle \varepsilon_{\mathrm{KWB}} \rangle = 7.3 \times 10^{-5}\,\mathrm{W\,kg^{-1}}$ for the August 2005 transect and $\langle \varepsilon_{\mathrm{obs}} \rangle = 3.8 \times 10^{-4}\,\mathrm{W\,kg^{-1}}$ and $\langle \varepsilon_{\mathrm{KWB}} \rangle = 2.4 \times 10^{-4}\,\mathrm{W\,kg^{-1}}$ for the May 2006 transect; Figs. 5, 6; Table 2).

Using the transect-average data, $\langle \varepsilon_{\mathrm{KWB}} \rangle$ is now compared to $\langle \varepsilon_{\mathrm{obs}} \rangle$ for all valid transects. The KWB parameterization slightly underpredicts ε (as exhibited by the difference between dashed and solid lines in Fig. 9b), with the linearized fit falling within a factor of 2 of the 1:1 line (Fig. 9b). However, the functional dependencies remain identical (Fig. 9b). The linearized least-squared fit between $\langle \varepsilon_{\mathrm{obs}} \rangle$ and $\langle \varepsilon_{\mathrm{KWB}} \rangle$ in $\log_{10}$ space yields a correlation coefficient of r = 0.72 with the slope of the best-fit line from a neutral regression statistically indistinguishable from 1, highlighting the variability in $\langle \varepsilon_{\mathrm{obs}} \rangle$ is being reasonably captured by the KWB parameterization (Fig. 9b).

Similar to $\langle \varepsilon_{\mathrm{obs}} \rangle / (\Delta u g')_\delta$, the observed values of $(L_o/L_\delta)^2$ also compare well to the KWB formulation in (7), which is to be expected since (6) and (7) only differ by a factor of $\mathrm{Ri}_b^{1/2}$ (Fig. 8c). The agreement between (7) and observed $(L_o/L_\delta)^2$ gives further credence to Kunze's (2014) argument that, for marginally unstable shear layers, the largest turbulence scales (L_o, L_T) are less than the thickness of the shear layer or turbulent patch; when L_o is larger than L_δ, it has been posited that fluid is entrained into the shear layer until $L_\delta = L_o$ (Kunze 2014). Note the variation in $(L_o/L_\delta)^2$ is largely dominated by the variability in L_o, as L_δ is generally restricted to the range $1.2\,\mathrm{m} \leq L_\delta \leq 3\,\mathrm{m}$. Altering the value of δ_h will only change the magnitude of $(L_o/L_\delta)^2$, not the fundamental Ri_b dependence.

c. *Consistency between KWB and a variable interfacial drag law formulation*

The $\langle \varepsilon_{\mathrm{obs}} \rangle$ is generally observed to decrease with increasing Ri_b (Fig. 8a); however, these two variables have different units, and hence the plot exhibits considerable scatter. For instance, the magnitude of $\langle \varepsilon_{\mathrm{obs}} \rangle$ from May 2006 is typically greater than the August 2005 data with similar Ri_b values, with the difference described by the term $N^3 L_\delta^2$ in (4).

To collapse $\langle \varepsilon_{\mathrm{obs}} \rangle$ onto a single curve, we return to the Imberger and Ivey (1991) scaling from MG04 in (1) and normalize $\langle \varepsilon_{\mathrm{obs}} \rangle$ by $(\Delta u g')_\delta$. Note again that, when evaluating the KWB parameterization, the relevant length scale is $L_\delta = h_p/\delta_h$. Scaling ε by $\mathrm{Ri}_b^{-1/2} N^3 L_\delta^2$ is advantageous because it removes the length-scale dependence and produces a nondimensional $\varepsilon/(\Delta u g')_\delta$ that can be directly compared to Ri_b.

Variability in $\langle \varepsilon_{\mathrm{obs}} \rangle / (\Delta u g')_\delta$ for similar Ri_b values is significantly reduced (as compared to Fig. 8a), with the higher N^2 May 2006 data now falling on the same general line as the data from the lower $\langle N^2 \rangle$ August 2005 sampling period (Fig. 8b). Importantly, $\langle \varepsilon_{\mathrm{obs}} \rangle / (\Delta u g')_\delta$ follows the theoretical KWB curve for the range $\mathrm{Ri}_b < \mathrm{Ri}_c$ for which KWB is valid, highlighting that the scaled dissipation is dependent on Ri_b (Fig. 8b). For low Ri_b regimes, the constant value initially assumed by

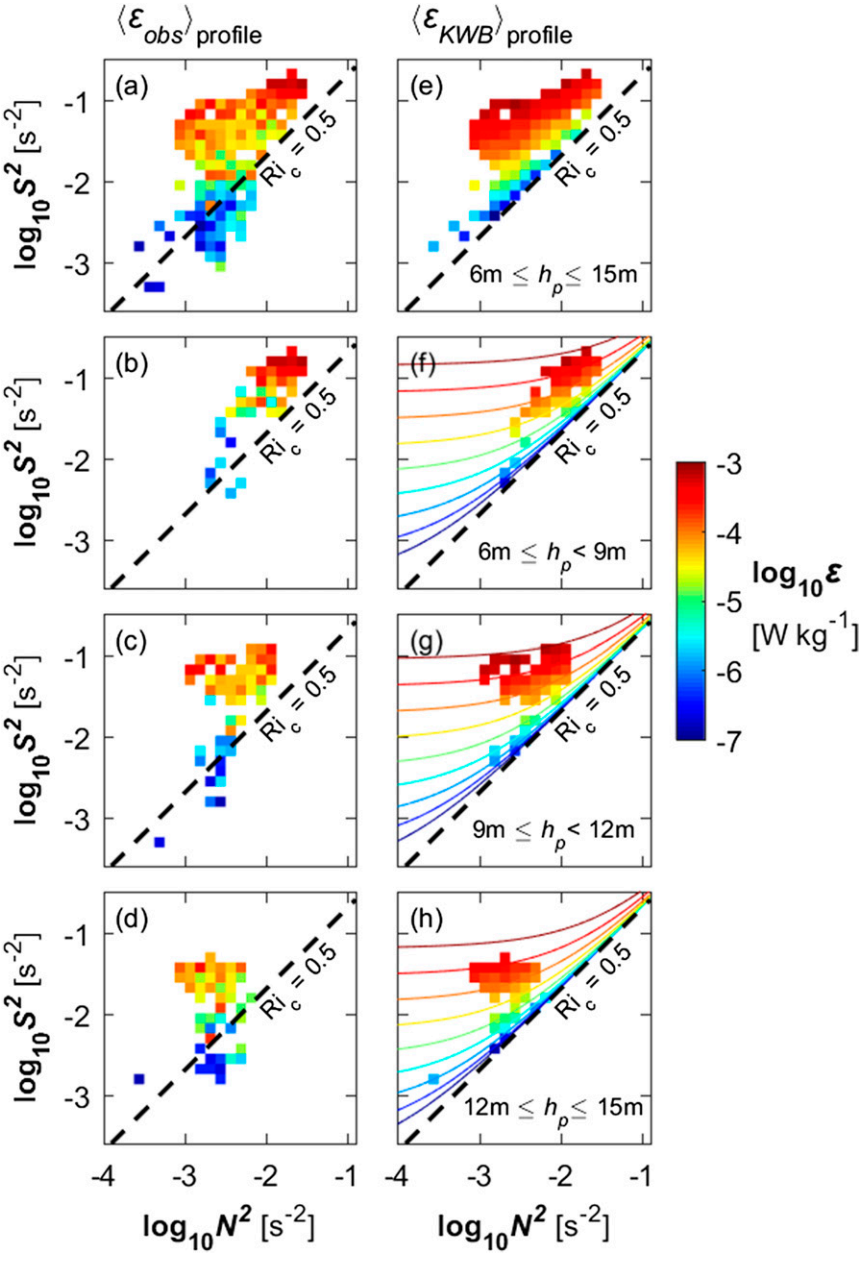

FIG. 7. Bin-averaged (left) $\langle \varepsilon_{\rm obs} \rangle_{\rm profile}$ and (right) $\langle \varepsilon_{\rm KWB} \rangle_{\rm profile}$ in $\log_{10}N^2$ and S^2 space with eight bins per decade and are separated by the plume depth ranges (a),(e) all h_p, (b),(f) $6 \le h_p < 9$ m, (c),(g) $9 \le h_p < 12$ m, and (d),(h) $12 \le h_p < 15$ m. Color contours in (f)–(h) are $\varepsilon_{\rm KWB}$ over the entire N^2 and S^2 parameter space using the respective median h_p value.

MGH07 multiplied by δ_h^2, $\varepsilon_c/(\Delta u g')_\delta = 0.05$ is consistent with our observations (Fig. 8b), though note that MacDonald and Chen (2012) later argued that this was a spreading impacted value. For higher Ri_b regimes the observations are one to two orders of magnitude smaller than the MGH07 value, residing closer to the nonspreading value from MacDonald and Chen (2012), even though (6) is solely a function of Ri_b and does not explicitly include a lateral spreading parameter (Fig. 8b).

6. Validity of constant $\varepsilon/(\Delta u g')$ and $C_{\rm di}$ assumptions

The use of $C_{\rm di} = 4.2 \times 10^{-4}$ in (2) unsurprisingly leads to an overestimate of ε in less energetic regions (Fig. 9a). Using (1) and estimating ε with a constant scaled

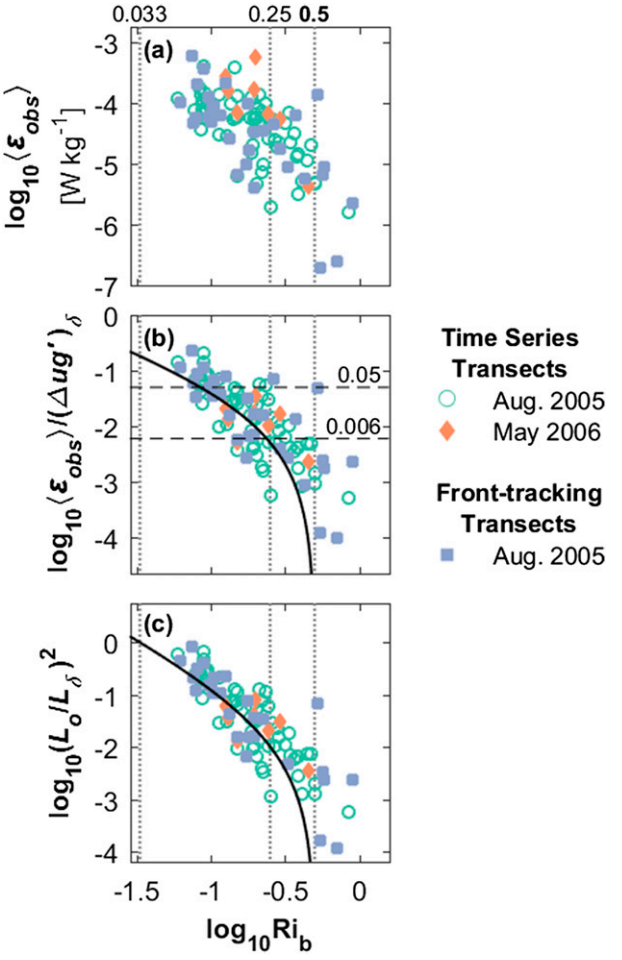

FIG. 8. Observed values of (a) $\langle \varepsilon_{obs} \rangle$, (b) $\langle \varepsilon_{obs} \rangle / (\Delta u g')_\delta$, and (c) $(L_o/L_\delta)^2$ plotted against Ri_b. Solid black line in (b) and (c) is the KWB estimate from (6) and (7), respectively. Black horizontal dashed lines in (b) mark the scaled values from MG04, $\varepsilon/(\Delta u g')_\delta = 0.05$, and MacDonald and Chen (2012), $\varepsilon/(\Delta u g')_\delta = 0.006$. Vertical dotted gray lines mark Ri_b values and are labeled above (a) with Ri_c in bold.

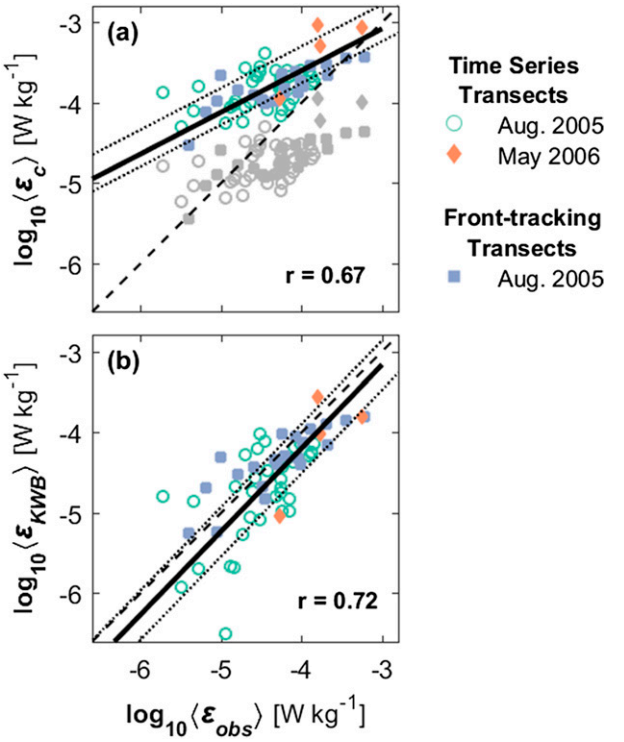

FIG. 9. Comparison between (a) $\langle \varepsilon_c \rangle$ and $\langle \varepsilon_{obs} \rangle$ and (b) $\langle \varepsilon_{KWB} \rangle$ and $\langle \varepsilon_{obs} \rangle$ for front-tracking and time series data. In (a), $\langle \varepsilon_c \rangle$ is estimated using $C_{di} = 4.2 \times 10^{-4}$ (colored symbols) and $C_{di} = 5 \times 10^{-5}$ (gray symbols). Dashed line is the 1:1 line, thick black line is the best fit from a linearized neutral regression, and the black dotted lines mark the region within a factor of 2 of the fit.

dissipation rate $\varepsilon = \Delta u g' (2 \times 10^{-3})$, as initially done by MGH07, similarly overestimates ε in less energetic regimes (not shown). To determine when $C_{di} = 4.2 \times 10^{-4}$ is valid, that is, when the effects of stratification can reasonably be neglected, we examine the dependencies of the scaled dissipation $\varepsilon/(\Delta u g')_\delta$ on N^2 and S^2. From (5) and (6), the KWB parameterizations for the interfacial drag C_{KWB} and scaled dissipation $\varepsilon_{KWB}/(\Delta u g')_\delta$ are solely functions of Ri_b. Near Ri_c, C_{KWB} rapidly increases as Ri_b decreases, then as $\mathrm{Ri}_b \ll \mathrm{Ri}_c$, C_{KWB} approaches a constant value of 1/96 (Fig. 10a). Once scaled by δ_h^2, $C_{di} = 4.2 \times 10^{-4}$, which is reasonably close to $C_{di} = 5 \times 10^{-4}$ estimated by MG04; $\varepsilon_{KWB}/(\Delta u g')_\delta$ increases rapidly near Ri_c as well but, in contrast to C_{KWB}, continues to increase even as $\mathrm{Ri}_b \ll \mathrm{Ri}_c$ (Fig. 10a).

From the theoretical ε_{KWB} contoured in Figs. 7f–h using (4), it is apparent that for $\mathrm{Ri}_b \ll \mathrm{Ri}_c$, the influence of N^2 on ε decreases, leaving S^2 as the dominant factor controlling ε. The N^2 dependence of ε_{KWB} can be shown by holding S^2 constant in (4), leaving Ri_b to vary only with N^2. The same exercise can be carried out by holding N^2 constant and only varying S^2, revealing the S^2 dependence of ε_{KWB}. This is analogous to taking horizontal (varying N^2) or vertical (varying S^2) slices through the theoretical ε_{KWB} contoured in N^2 and S^2 space in Fig. 7f. The N^2-dependent ε_{KWB} displays a similar structure to C_{KWB}, rapidly increasing near Ri_c and then as $\mathrm{Ri}_b \ll \mathrm{Ri}_c$ levels off with ε_{KWB} changing little as N^2 decreases (Fig. 10b). The structure of the S^2-dependent ε_{KWB} is similar to that of $\varepsilon_{KWB}/(\Delta u g')_\delta$, increasing rapidly near Ri_c and then continuing to increase as $\mathrm{Ri}_b \ll \mathrm{Ri}_c$ (Fig. 10c).

Taken together, the N^2 and S^2 dependencies of ε_{KWB} reveal that as Ri_b decreases to the point where $\mathrm{Ri}_b \ll \mathrm{Ri}_c$, S^2 dominates the KWB parameterization and N^2 can be neglected. To make this clearer, the KWB parameterization in (4) can be rearranged into the form

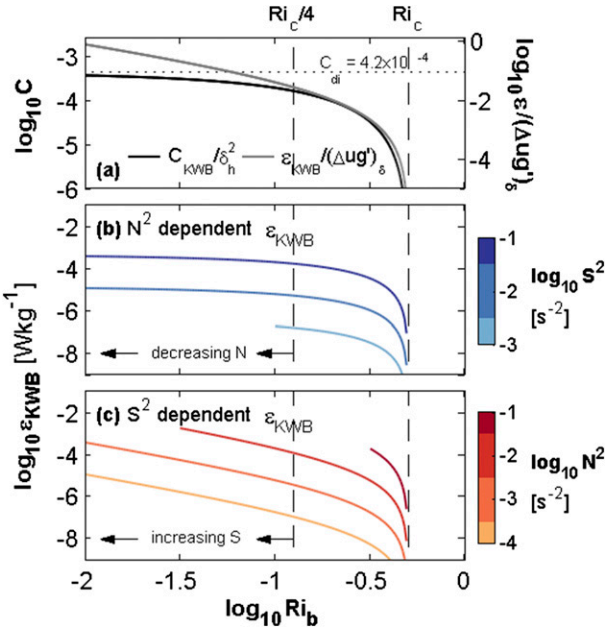

FIG. 10. (a) The $C_{\mathrm{KWB}}/\delta_h^2$ and $\varepsilon_{\mathrm{KWB}}/(\Delta u g')_\delta$ with respect to Ri_b. (b), (c) The $\varepsilon_{\mathrm{KWB}}$ plotted against Ri_b. For each line plotted in (b) S^2 is constant with Ri_b only varying with N^2 and in (c) N^2 is constant for each line with Ri_b only varying with S^2; $\varepsilon_{\mathrm{KWB}}$ is computed using $L_\delta = 1.25$. The vertical black dashed lines mark the locations of Ri_c and $\mathrm{Ri}_c/4$.

$$\varepsilon_{\mathrm{KWB}} = (1 - \mathrm{Ri}_f)S^3 L_\delta^2 \frac{(1 - \mathrm{Ri}_b/\mathrm{Ri}_c)[1 - (\mathrm{Ri}_b/\mathrm{Ri}_c)^{-1/2}]}{96}. \tag{8}$$

When $\mathrm{Ri}_b/\mathrm{Ri}_c \ll 1$, $\varepsilon_{\mathrm{KWB}} \cong (1 - \mathrm{Ri}_f)S^3 L_\delta^2/96$. Assuming a linear velocity profile and $L_\delta = h_p/\delta_h$ with $\delta_h = 5$, this expression is further reduced to $\varepsilon_{\mathrm{KWB}} = (1 - \mathrm{Ri}_f)(\Delta u^3/h_p)(4.2 \times 10^{-4})$. The drag coefficient $C_{\mathrm{di}} = 4.2 \times 10^{-4}$ is equivalent to that in Fig. 10a.

So how small does Ri_b have to be before the constant drag formulation ($C_{\mathrm{di}} = 4.2 \times 10^{-4}$) can be used? To define this region explicitly, the ratio of $\langle\varepsilon_c\rangle/\langle\varepsilon_{\mathrm{obs}}\rangle$ is compared to $\mathrm{Ri}_b/\mathrm{Ri}_c$ (Fig. 11a). When $\mathrm{Ri}_b < \mathrm{Ri}_c/4$, $\langle\varepsilon_c\rangle/\langle\varepsilon_{\mathrm{obs}}\rangle$ is close to unity, while, during periods when $\mathrm{Ri}_b > \mathrm{Ri}_c/4$, $\langle\varepsilon_c\rangle/\langle\varepsilon_{\mathrm{obs}}\rangle$ is larger than one. The ratio of $\langle\varepsilon_c\rangle/\langle\varepsilon_{\mathrm{obs}}\rangle$ in the larger Ri_b regions signifies that the constant C_{di} formulation does not properly capture the influence of the stratification on ε; on average the constant drag formulation overestimates ε by nearly a factor of 5 for the observations presented here. When $\mathrm{Ri}_b < \mathrm{Ri}_c/4$, S^2 dominates the variability in ε and N^2 can be neglected (Figs. 10, 11a). It is in this energetic region that $C_{\mathrm{di}} = 4.2 \times 10^{-4}$ is reasonably valid. Note that the analysis presented here of a constant C_{di} formulation has been carried out using a single value of the drag coefficient $C_{\mathrm{di}} = 4.2 \times 10^{-4}$, and thus the reported range of Ri_b values where the formulation is valid is dependent on the chosen value of C_{di}. The $C_{\mathrm{di}} = 4.2 \times 10^{-4}$ arises in the weakly stratified $\mathrm{Ri}_b \to 0$ limit, that is, when stratification N^2 is unimportant.

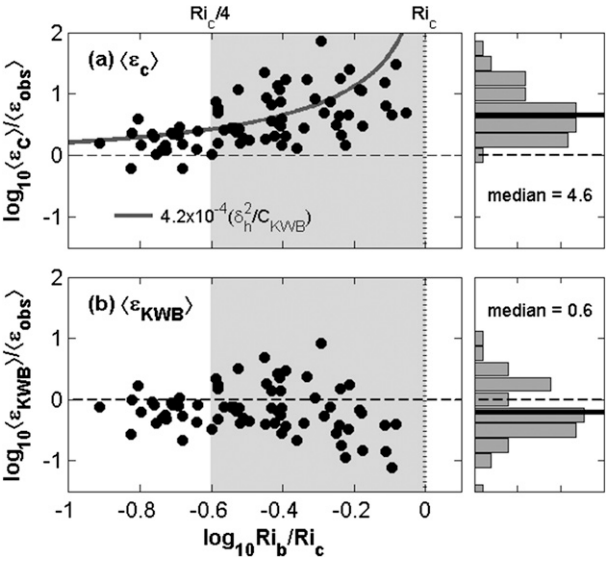

FIG. 11. Ratio of (a) $\langle\varepsilon_c\rangle/\langle\varepsilon_{\mathrm{obs}}\rangle$ and (b) $\langle\varepsilon_{\mathrm{KWB}}\rangle/\langle\varepsilon_{\mathrm{obs}}\rangle$ plotted with respect to $\mathrm{Ri}_b/\mathrm{Ri}_c$, with $\mathrm{Ri}_c = 0.5$. Dark gray line in (a) is the ratio between $C_{\mathrm{di}} = 4.2 \times 10^{-4}$ and $C_{\mathrm{KWB}}/\delta_h^2$. Right panels are the normalized histograms of the ratios over the range, $\mathrm{Ri}_c/4 < \mathrm{Ri}_b < \mathrm{Ri}_c$, highlighted by the gray shaded region in (a) and (b). The median value over the range is marked by the thick black line in the histogram plots.

The ratios of the KWB estimates and observations, $\langle\varepsilon_{\mathrm{KWB}}\rangle/\langle\varepsilon_{\mathrm{obs}}\rangle$, are plotted in Fig. 11b for comparison. The KWB parameterization, with $\delta_h = 5$ and $\mathrm{Ri}_c = 0.5$, slightly underpredicts ε, and there is a noticeable decrease in accuracy when $\mathrm{Ri}_b \geq (2/3)\mathrm{Ri}_c$. Overall, the KWB parameterization more closely tracks the observations than the interfacial drag formulation with $C_{\mathrm{di}} = 4.2 \times 10^{-4}$ (Figs. 9, 11). The median value for $\langle\varepsilon_{\mathrm{KWB}}\rangle/\langle\varepsilon_{\mathrm{obs}}\rangle$ is 0.6 over $\mathrm{Ri}_b < \mathrm{Ri}_c/4$ (Fig. 11b), consistent with Polzin (1996) who reported that the KWB parameterization underpredicted ε by a factor of 0.57 for their set of open-ocean observations when using $\mathrm{Ri}_c = 0.4$. The decrease in $\langle\varepsilon_{\mathrm{KWB}}\rangle/\langle\varepsilon_{\mathrm{obs}}\rangle$ when $\mathrm{Ri}_b \geq (2/3)\mathrm{Ri}_c$ signifies the breakdown of the KWB parameterization in this region that is likely due to the KWB parameterization requiring $\varepsilon = 0$ at $\mathrm{Ri}_b \geq \mathrm{Ri}_c$. In reality, turbulence still continues to exist, even at $\mathrm{Ri}_b > \mathrm{Ri}_c$, albeit at lower levels. This is likely due to the presence of decaying turbulence or turbulence generated at scales not captured by a finescale parameterization (e.g., Rohr et al. 1988; Itsweire et al. 1993; Polzin 1996; Smyth et al. 2001).

7. Conclusions

Here, we have used direct observations of ε over a wide range of N^2, S^2 parameter space to examine the

effects of the stratification and shear on turbulence in a tidal river plume system. Specifically, the large dynamic range of the observations has permitted us to quantify the effects of stratification that were not possible to identify in previous tidal plume studies (MG04; MGH07).

We find that turbulent dissipation in the tidal Columbia River plume are related to the local, bulk-averaged shear, stratification, and plume thickness alone, motivating the application of a turbulence parameterization described by KWB. Direct estimates of ε collected in the tidal plume of the Columbia River have been compared to those predicted through this parameterization, and it is found that the KWB parameterization captures the observed variability in ε remarkably well (Figs. 8, 9). The results presented here highlight importance of reduced shear and h_p in controlling turbulence intensity in strongly stratified and sheared systems.

The observed normalized dissipation rate $\varepsilon/(\Delta u g')$ displays a clear Ri_b dependence and falls along the curve predicted by the KWB parameterization. Similarly, C_{KWB} is found to be strongly dependent on Ri_b, particularly in the range $\mathrm{Ri}_c/4 < \mathrm{Ri}_b < \mathrm{Ri}_c$. As Ri_b becomes smaller than $\mathrm{Ri}_c/4$, C_{KWB} approaches an asymptotic value (Fig. 10a). Thus, in the more energetic regions of N^2, S^2 parameter space where $\mathrm{Ri}_b \ll \mathrm{Ri}_c$, C_{KWB} is relatively constant, and $\varepsilon_{\mathrm{KWB}}$ and $\varepsilon_{\mathrm{KWB}}/(\Delta u g')_\delta$ are independent of N^2, depending only on S^2, h_p, and C_{di} (Fig. 10). Our observations suggest the upper-limit $C_{\mathrm{di}} = 4.2 \times 10^{-4}$ is valid for $\mathrm{Ri}_b < \mathrm{Ri}_c/4$ (Fig. 11). However, when $\mathrm{Ri}_b > \mathrm{Ri}_c/4$, the role of N^2 in damping production must be accounted for to predict ε. Extending on the previous works, a Ri_b-dependent interfacial drag coefficient C_{KWB} and scaled dissipation rate $\varepsilon_{\mathrm{KWB}}/(\Delta u g')_\delta$ can be defined to adequately capture the Ri_b variability in ε for the tidal Columbia River plume.

It has been reported that the drag coefficient for bottom gravity currents depends, in part, on the entrainment of the lower-momentum ambient fluid into the gravity current, with the entrainment expressed as a vertical entrainment velocity w_e and nondimensionally as $E = w_e/u$ (Dallimore et al. 2001; Arneborg et al. 2007; Umlauf et al. 2007). Recent laboratory studies of a spreading river plume (Yuan and Horner-Devine 2013), in addition to historical studies of gravity currents (i.e., Ellison and Turner 1959; Christodoulou 1986; Cenedese and Adduce 2010), have shown that E displays a strong functional dependence on some form of the Richardson number of the flow. Interestingly, the Ri dependence of the empirical entrainment laws like that from Ellison and Turner (1959) (not shown) bear a striking similarity to that of C_{KWB} in (5). Here, we speculate that the KWB parameterization should be generally applicable in describing the turbulence and mixing in more general unstable and marginally unstable gravity-driven flows while possibly providing a more dynamically relevant reasoning for the observed Ri dependence of E than these previous studies.

Direct measurements of ε in tidal plume systems can be difficult and expensive to collect and analyze. We find here that the KWB parameterization is advantageous in these more marginally unstable cases because it only requires knowledge of the vertical gradients of density and velocity. While the inclusion of a lateral spreading parameter (MacDonald and Chen 2012) is not part of the KWB parameterization, more work is needed to determine the role of the aspect ratio in driving the disparity in the lateral spreading influence in the Columbia and Merrimack tidal plumes.

Perhaps the biggest weakness of the KWB parameterization is the somewhat arbitrary choice of L_δ (Kunze 2014). Additional work is required to more properly define L_δ in addition to more thorough examinations of the assumption of a constant-flux Richardson number and the proper value of the critical Richardson number. Even so, the results presented here appear to be robust and promising and are likely applicable to many other unstable and marginally unstable stratified flows, such as generic gravity currents and deep overflows.

Acknowledgments. W. D. Smyth, the OSU Ocean Mixing group provided valuable comments on the manuscript. E. Kunze and D. G. MacDonald contributed very thoughtful reviews that greatly improved the manuscript. We also thank A. Perlin, R. Kreth, and M. Neeley-Brown for their technical expertise, along with the captain and crew of the R/V *Point Sur* for making data collection possible. Hans Moritz and the U.S. Army Corps of Engineers kindly provided the tidal data from the MCR mooring. Funding for the data collection was provided by NSF Grant OCE-0238727. J. T. Jurisa's work was funded through NSF Grant OCE-1131621.

REFERENCES

Arneborg, L., V. Fiekas, L. Umlauf, and H. Burchard, 2007: Gravity current dynamics and entrainment—A process study based on observations in the Arkina Basin. *J. Phys. Oceanogr.*, **37**, 2094–2112, doi:10.1175/JPO3110.1.

Cenedese, C., and C. Adduce, 2010: A new parameterization for entrainment in overflows. *J. Phys. Oceanogr.*, **40**, 1835–1850, doi:10.1175/2010JPO4374.1.

Christodoulou, G. C., 1986: Interfacial mixing in stratified flows. *J. Hydraul. Res.*, **24**, 77–92, doi:10.1080/00221688609499323.

Dallimore, C. J., J. Imberger, and T. Ishikawa, 2001: Entrainment and turbulence in saline underflow in Lake Ogawara. *J. Hydraul. Eng.*, **127**, 937–948, doi:10.1061/(ASCE)0733-9429(2001)127:11(937).

Ellison, T. H., and J. S. Turner, 1959: Turbulent entrainment in stratified flows. *J. Fluid Mech.*, **6**, 423–448, doi:10.1017/S0022112059000738.

Geyer, W. R., and D. M. Farmer, 1989: Tide-induced variation of the dynamics of a salt wedge estuary. *J. Phys. Oceanogr.*, **19**, 1060–1072, doi:10.1175/1520-0485(1989)019<1060:TIVOTD>2.0.CO;2.

——, A. C. Lavery, M. E. Scully, and J. H. Trowbridge, 2010: Mixing by shear instability at high Reynolds number. *Geophys. Res. Lett.*, **37**, L22607, doi:10.1029/2010GL045272.

Hazel, P., 1972: Numerical studies of the stability of inviscid stratified shear flows. *J. Fluid Mech.*, **51**, 39–61, doi:10.1017/S0022112072001065.

Hetland, R. D., 2010: The effects of mixing and spreading on density in near-field river plumes. *Dyn. Atmos. Oceans*, **49**, 37–53, doi:10.1016/j.dynatmoce.2008.11.003.

Hickey, B. M., and Coauthors, 2010: River influences on shelf ecosystems: Introduction and synthesis. *J. Geophys. Res.*, **115**, C00B17, doi:10.1029/2009JC005452.

Imberger, J., and G. N. Ivey, 1991: On the nature of turbulence in a stratified fluid. Part II: Application to lakes. *J. Phys. Oceanogr.*, **21**, 659–680, doi:10.1175/1520-0485(1991)021<0659:OTNOTI>2.0.CO;2.

Itsweire, E. C., J. R. Koseff, D. A. Briggs, and J. H. Ferziger, 1993: Turbulence in stratified shear flows: Implications for interpreting shear-induced mixing in the ocean. *J. Phys. Oceanogr.*, **23**, 1508–1522, doi:10.1175/1520-0485(1993)023<1508:TISSFI>2.0.CO;2.

Ivey, G. N., and J. Imberger, 1991: On the nature of turbulence in a stratified fluid. Part I: The energetics of mixing. *J. Phys. Oceanogr.*, **21**, 650–658, doi:10.1175/1520-0485(1991)021<0650:OTNOTI>2.0.CO;2.

Kilcher, L. F., and J. D. Nash, 2010: Structure and dynamics of the Columbia River tidal plume front. *J. Geophys. Res.*, **115**, C05S90, doi:10.1029/2009JC006066.

——, ——, and J. N. Moum, 2012: The role of turbulence stress divergence in decelerating a river plume. *J. Geophys. Res.*, **117**, C05032, doi:10.1029/2011JC007398.

Kunze, E., 2014: The relation between unstable shear layer thickness and turbulence length scales. *J. Mar. Res.*, **72**, 95–104, doi:10.1357/002224014813758977.

——, A. J. Williams III, and M. G. Briscoe, 1990: Observations of shear and vertical stability from a neutrally buoyant float. *J. Geophys. Res.*, **95**, 18 127–18 142, doi:10.1029/JC095iC10p18127.

MacDonald, D. G., and W. R. Geyer, 2004: Turbulent energy production and entrainment at a highly stratified estuarine front. *J. Geophys. Res.*, **109**, C05004, doi:10.1029/2003JC002094.

——, and F. Chen, 2012: Enhancement of turbulence through lateral spreading in a stratified shear flow: Development and assessment of a conceptual model. *J. Geophys. Res.*, **117**, C0525, doi:10.1029/2011JC007484.

——, L. Goodman, and R. D. Hetland, 2007: Turbulent dissipation in a near-field river plume: A comparison of control volume and microstructure observations with a numerical model. *J. Geophys. Res.*, **112**, C07026, doi:10.1029/2006JC004075.

MacKinnon, J. A., and M. C. Gregg, 2005: Spring mixing: Turbulence and internal waves during restratification on the New England shelf. *J. Phys. Oceanogr.*, **35**, 2425–2443, doi:10.1175/JPO2821.1.

Miles, J. W., 1961: On the stability of heterogeneous shear flows. *J. Fluid Mech.*, **10**, 496–508, doi:10.1017/S0022112061000305.

Moum, J. N., M. Gregg, R. C. Lien, and M. E. Carr, 1995: Comparison of turbulent kinetic energy dissipation rate estimates from two oceanic microstructure profilers. *J. Atmos. Oceanic Technol.*, **12**, 346–366, doi:10.1175/1520-0426(1995)012<0346:COTKED>2.0.CO;2.

Nash, J. D., L. F. Kilcher, and J. N. Moum, 2009: Structure and composition of a strongly stratified tidally pulsed river plume. *J. Geophys. Res.*, **114**, C00B12, doi:10.1029/2008JC005036.

Peters, H., M. C. Gregg, and T. B. Sanford, 1995: On the parameterization of equatorial turbulence: Effect of fine-scale variations below the range of the diurnal cycle. *J. Geophys. Res.*, **100**, 18 333–18 348, doi:10.1029/95JC01513.

Polzin, K., 1996: Statistics of the Richardson number: Mixing models and finestructure. *J. Phys. Oceanogr.*, **26**, 1409–1425, doi:10.1175/1520-0485(1996)026<1409:SOTRNM>2.0.CO;2.

Rohr, J. J., E. C. Itsweire, K. N. Helland, and C. W. Van Atta, 1988: Growth and decay of turbulence in a stably stratified shear flow. *J. Fluid Mech.*, **195**, 77–111, doi:10.1017/S0022112088002332.

Smyth, W. D., J. N. Moum, and D. R. Caldwell, 2001: The efficiency of mixing in turbulent patches: Inferences from direct simulations and microstructure observations. *J. Phys. Oceanogr.*, **31**, 1969–1992, doi:10.1175/1520-0485(2001)031<1969:TEOMIT>2.0.CO;2.

Thompson, R. O. R. Y., 1980: Efficiency of conversion of kinetic energy and potential energy by breaking internal waves. *J. Geophys. Res.*, **85**, 6631–6635, doi:10.1029/JC085iC11p06631.

Thorpe, S. A., 2010: Breaking internal waves and turbulent dissipation. *J. Mar. Res.*, **68**, 851–880, doi:10.1357/002224010796673876.

Umlauf, L., L. Arneborg, H. Burchard, V. Fiekas, H. U. Lass, V. Mohrholz, and H. Prandke, 2007: Transverse structure of turbulence in a rotating gravity current. *Geophys. Res. Lett.*, **34**, L08601, doi:10.1029/2007GL029521.

Yuan, Y., and A. R. Horner-Devine, 2013: Laboratory investigation of the impact of lateral spreading on buoyancy flux in a river plume. *J. Phys. Oceanogr.*, **43**, 2588–2610, doi:10.1175/JPO-D-12-0117.1.